Available online at www.sciencedirect.com
ScienceDirect
International Journal of Heat and Mass Transfer 50 (2007) 1328–1343
International Journal of HEAT and MASS TRANSFER
www.elsevier.com/locate/ijhmt

A 3-dimensional, coupled, DNS, heat transfer model and solution for multi-hole cooling

Fengquan Zhong, Garry L. Brown *

Department of Mechanical and Aerospace Engineering, Princeton University, Princeton, NJ 08544, USA

Received 5 January 2006; received in revised form 15 September 2006
Available online 28 November 2006

Abstract

A 3-dimensional, coupled, heat transfer model and solution for multi-hole cooling is described in this paper. It couples DNS calculations of the primary turbulent flow, the backside flow and the flow in the injection holes by solving the 3-D heat conduction equation for the wall with a mixed boundary condition, which leads to an iteration process to obtain a converged solution for the mean temperature in the wall and in the flow. The model is tested for both a laminar and a turbulent primary flow and the results show that the convergence to the solution is very efficient. The results obtained with this 3-D model are presented and compared with an adiabatic and a 1-D, conducting-wall, model. A non-dimensional parameter (Biot number) representing the relative importance of in-plane heat conduction in the wall is discussed. The cooling effectiveness predicted by the 3-D model is compared with experimental results at the same Reynolds number and satisfactory agreement is achieved.

Keywords: 3-Dimensional coupled heat transfer model; Direct numerical simulation (DNS); In-plane heat conduction

1. Introduction

Modern gas turbine design, for example, seeks higher efficiency and lower emissions and consequently more uniform temperatures in the combustor and less compressed gas used as a coolant are desirable goals. An important challenge then is to improve the efficiency of the cooling system for the combustor liner. A multi-hole cooling system (also called an "effusion cooling" system), especially with a light weight ceramic matrix composite (CMC), seems a promising cooling method for combustor liner protection. (A woven CMC is relatively easily provided with an arbitrarily large number of cooling holes located at the interstices of the weave.) By comparison with traditional discrete, film cooling, a multi-hole cooling system that has a hole geometry and spacing which, compared with a boundary layer thickness, more nearly approaches transpiration cooling, would obtain a more uniform surface temperature and achieve a higher cooling efficiency with cooling optimization. As we will see in this paper, a multi-hole cooling system can make good use of the cooling effects produced by the backside coolant flow and the coolant flow through the injection holes.

With the development of computational capacity, it seems possible, at low Reynolds number, to undertake a direct numerical simulation of a multi-hole cooling system, which is based on a DNS calculation of the flow fields with some efficient technique (to be found, and the subject of this paper) for coupling these flows through the heat conduction in the wall. The interaction of the primary hot flow with the injected secondary coolant flow has been the main issue investigated in most previous numerical studies. Adiabatic cooling effectiveness has been chosen, typically, to evaluate the cooling performance for different flow conditions and geometrical features of the cooling system. In reality, however, due to the thermal conductivity of the

* Corresponding author. Tel.: +1 609 258 6083; fax: +1 609 258 2404.
E-mail address: glb@Princeton.edu (G.L. Brown).

0017-9310/$ - see front matter © 2006 Elsevier Ltd. All rights reserved.
doi:10.1016/j.ijheatmasstransfer.2006.09.017

Nomenclature

d	hydraulic diameter
h	heat transfer coefficient
k	thermal conductivity
M	blowing ratio defined as mass flow rate ratio of coolant to primary flow: $\frac{(\rho v)_c}{(\rho u)_\infty}$
P	hole to hole lateral distance
q	heat flux
Re, Re_x	Reynolds number defined by stream wise distance and free stream velocity
Re_θ	Reynolds number defined by the boundary layer momentum thickness (θ in the usual notation) and the free stream velocity
S	hole to hole downstream distance
St	Stanton number $St = \frac{h}{\rho u C_p}$
t	wall thickness
T	temperature
u, v, w	velocity components
x, y, z	streamwise, normal, spanwise direction
u_τ	mean turbulent boundary layer friction velocity immediately upstream of the multi-hole cooling

Greek symbols

$\delta_{0.99}$	boundary layer thickness
θ	cooling effectiveness defined by $\theta = \frac{T_\infty - T_{\text{cooling-surface}}}{T_\infty - T_{\text{coolant}}}$
ρ	density
ν	kinetic viscosity

Subscript and superscripts

1, 2, 3	upper wall surface, lower wall surface, hole inner surface
aw	adiabatic wall
c	coolant
h	hole
rms	root mean square
w	wall
+	non-dimensional lengths scaled by $\frac{\nu}{u_\tau}$
∞	free stream

wall material, a multi-hole cooling system consists of three cooling effects, as illustrated in Fig. 1. They are: (1) the reduction of the wall temperature for an adiabatic wall as a direct result of the coolant jets; (2) the conduction of heat through the wall due to the thermal conductivity of the wall material and the heat transfer to the backside flow (i.e. "backside cooling"); (3) the heat transfer to the coolant flow from the inner surface of the injection holes when coolant passes through the holes (i.e. "internal cooling"). The relative importance of each effect depends critically on the geometrical features of the wall and the operating conditions (e.g. static pressure, flow rates, etc.) of the cooling system. The direct effect of the coolant jet, which is often evaluated by using an adiabatic wall, has been investigated widely as in Lin et al. [1] and Fric et al. [2], and it is a dominant effect at high blowing ratio ($M \geqslant 1$). The other two effects, however, can be more important for a high efficiency, low blowing ratio cooling system, such as a multi-hole cooling system for multi-hole CMC materials that can have a relatively large number of holes and percentage open area with minimal cost penalty.

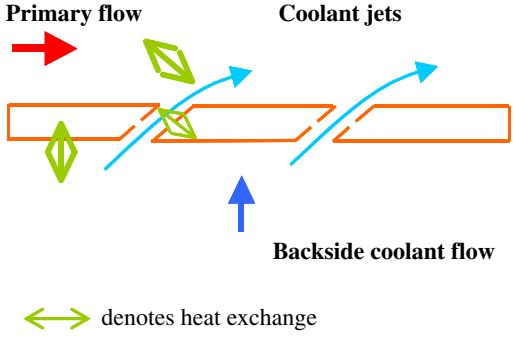

Fig. 1. A schematic view of a typical multi-hole cooling system.

Various experimental and numerical studies of backside cooling and/or internal cooling have been reported in the literature. Leger et al. [3] measured the overall cooling effectiveness, including the backside and internal cooling effects, for a multi-hole metal plate and the results in their case showed that the backside cooling effect accounted for approximately two thirds of the total cooling effectiveness. Martiny et al. [4] used a theoretical model to investigate the heat absorption occurring inside the holes and on the backside surface and documented a significant rise in coolant temperature through the hole. The backside and internal cooling effect contributed half of the total cooling effect in their case.

A Direct Numerical Simulation (DNS), which approximately couples the heat transfer to and from all surfaces, was reported by Zhong and Brown [5]. They coupled the heat transfer by proposing a local 1-D coupled model. Based on the weak dependence of the backside heat transfer coefficient, h_2, on the primary flow, and the linearity of the heat conduction in the wall, the fully coupled problem was simplified into a set of iterations in which the primary and the backside flow were separately and alternately calculated. With the key assumption that the heat flux through the wall is locally 1-D, a new thermal boundary condition, which coupled the two flows, was derived and used to solve the primary flow. In terms of the geometry and variables in Fig. 2, we summarize here the main steps taken to obtain this thermal boundary condition:

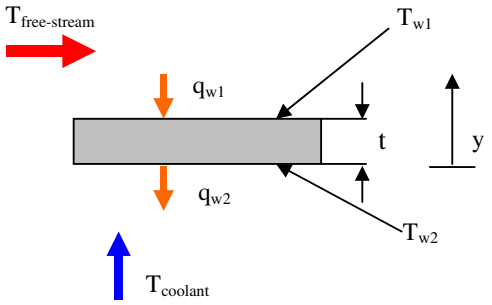

Fig. 2. Heat flux on both sides of the wall for the 1-D wall model.

$$q_{w1} = q_{w2} = k_w \frac{T_{w1} - T_{w2}}{t} \tag{1}$$

$$q_{w1} = k_1 \left.\frac{\partial T}{\partial y}\right|_{w1} \tag{2}$$

$$q_{w2} = h_2 (T_{w2} - T_c) \tag{3}$$

Combining (1)–(3), we obtain

$$\left.\frac{\partial T}{\partial y}\right|_{w1} = \frac{1}{k_1} \frac{T_{w1} - T_c}{\frac{1}{h_2} + \frac{t}{k_w}} \tag{4}$$

This provides a mixed boundary condition for the flow in the region above the wall. The iteration process they used to obtain a solution is illustrated below in Part A of Fig. 4; it was found to converge quickly to a mean surface temperature on both sides of the wall for both laminar and turbulent primary flows.

The assumption of one dimensionality for the local heat flux through the wall will be increasingly inaccurate, however, near the injection holes, where in-plane heat conduction will occur. Neglecting the in-plane heat conduction would lead to an over-prediction of the temperature variation on the cooling surface, since this variation would be reduced by the actual in-plane heat conduction. In this paper, a 3-D coupled heat transfer model, which models the actual steady heat conduction in the wall (assuming only a given distribution of heat conductivity), is developed. The basic iteration process used by Zhong and Brown [5] for the primary and backside flows is used but the 3-D temperature distribution in the solid wall is calculated directly by solving the steady 3-D heat conduction equation. A mixed boundary condition, related to the surface temperature and the calculated local heat transfer coefficient on both the upper and lower surfaces and on the inner surface of each hole is introduced and used when solving the heat conduction equation. It is shown in the present paper that the boundary conditions that are used can guarantee the uniqueness of the solution for the steady heat conduction equation. Consequently, the iteration process is found to be highly efficient. The converged solution can be obtained within three iteration steps. In this paper, the 3-D coupled model, including the mixed boundary conditions and the modified iteration procedure, is described and the results obtained are compared with an adiabatic wall model and with the simpler 1-D coupled model. We have also done experiments on multi-hole cooling with CMC materials. This experimental work has used the facility described in Zhong and Brown [5] and is in progress but we include some experimental results here at conditions that duplicate those of the DNS calculations. The comparison between the predictions and the experimental data shows good agreement.

2. The 3-dimensional, coupled model

2.1. Description of the multi-hole cooling problem

As shown in Fig. 1, a multi-hole cooling system consists of two flow regions, one above the wall and the other below and through it, which, in principle, are coupled at all times at the flow interface through continuity in pressure, velocity and temperature and their spatial derivatives. In this paper the two flow regions are coupled through continuity in the mean velocity components and the mean temperature profile at the exit of the hole. The mean temperature on the wall surface and corresponding mean heat flux to the wall must satisfy the steady, 3-D, heat conduction equation. Thus the two flow regions are also coupled with each other via the 3-D solid wall or we may say that the temperature and heat flux inside the 3-D wall is determined by the flow and thermal properties in these two flow regions. How best to solve the heat conduction equation with the thermal information obtained from the fluid flow is the key point.

Considering the linearity of the heat conduction in the wall, a fully coupled fluid–solid heat transfer problem can be simplified into a decoupled iteration procedure based on solving alternately the equations for the fluid flows and for the solid wall. The thermal interaction between the fluid flow and solid wall requires continuity in the temperature and heat flux across the fluid–solid interface. In this paper, instead of iterating to try and match temperature and heat flux directly at the fluid–solid interface as used in conventional heat transfer coupling, a mixed thermal boundary condition, governed by the calculated heat transfer coefficients of both the primary and backside flows, is used; it is expected to speed up the convergence to the solution.

2.2. Mixed boundary conditions for the 3-D wall solution

We expect the heat transfer coefficient, $h = \frac{q_w}{\Delta T}$, to depend weakly on the actual temperature at the wall for a specific flow field, so using it instead of q_w or T_w to couple the fluid and solid regimes would substantially improve the speed of convergence. Fig. 3 shows the boundary conditions used in the 3-D coupled model; the mixed boundary conditions for the wall arise from the definition of a heat transfer coefficient as follows:

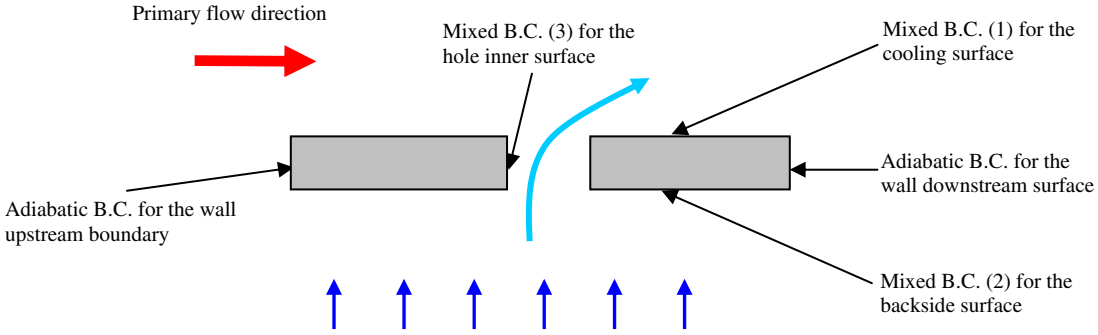

Fig. 3. Boundary conditions used for solving the wall temperature.

$$\text{Mixed BC (1)}: \quad -\nabla T\cdot\vec{n}|_{w1} = -\left.\frac{\partial T}{\partial n}\right|_{w1} = \frac{h_1}{k_w}(T_{w1}-T_\infty) \quad (5)$$

$$\text{Mixed BC (2)}: \quad -\nabla T\cdot\vec{n}|_{w2} = -\left.\frac{\partial T}{\partial n}\right|_{w2} = \frac{h_2}{k_w}(T_{w2}-T_c) \quad (6)$$

$$\text{Mixed BC (3)}: \quad -\nabla T\cdot\vec{n}|_{w3} = -\left.\frac{\partial T}{\partial n}\right|_{w3} = \frac{h_3}{k_w}(T_{w3}-T_h) \quad (7)$$

where $h_1 = \frac{q''_{w1}}{T_{w1}-T_\infty}$,[1] $h_2 = \frac{q''_{w2}}{T_{w2}-T_c}$, $h_3 = \frac{q''_{w3}}{T_{w3}-T_h}$ and $\vec{n}$ is the surface normal vector and where T_c is the temperature of the coolant and T_h is determined from the average centerline temperature of the coolant over the length of the hole and where q''_w is the heat flux at the surface, calculated in the fluid, at each iteration.

An adiabatic wall condition is used initially for the upstream and downstream boundaries of the wall as in Fig. 3. A symmetry boundary condition is used initially in the spanwise direction for laminar flow cases and in the turbulent cases a periodic condition.

The mixed boundary condition gives a unique solution for the Laplace equation for the specific case when the heat transfer coefficients, h_1, h_2, h_3 defined above, are all positive (see Appendix A for the proof). Negative heat transfer coefficients, however, can physically exist on some regions of the surface; for example h_1 can be negative in a small region just downstream of the injection hole where the wall is locally hotter than the flow that is near the surface (as is evident in Fig. 18 for a calculated h_1). In such a negative-h_1 region, locally we replace the mixed boundary condition by the calculated q''_{w1}. We discuss this case also in Appendix A and prove that this approach (i.e. the mixed boundary condition everywhere except where the surface heat flux is used in the small regions where $h_1 < 0$) gives a unique solution for the temperature field and heat flux in the wall. This is the basic methodology that is used in all of the following calculations.

[1] *Note*: If instead h_1 is defined as $h_1 = \frac{q''_{w1}}{T_{w1}-T_{aw}}$, then it is clear that as $T_{w1} - T_{aw}$ goes to zero (and goes negative because of the in-plane heat conduction, for example), h_1 will, in general, be subject to large fluctuations with each iteration for T_{w1}. This will lead to slow convergence. While the uniqueness argument (Appendix A) still applies since T_{aw} is a given function on the cooling surface of the wall, this definition would not overcome the fact that h_1 can become negative due to the in-plane heat conduction. It is therefore preferable in this context to define h_1 as in (5), since T_{w1} is always less than T_∞. By this definition, large fluctuations in h_1 with each iteration are avoided.

2.3. Iteration procedure

The iteration process has two principal parts: the first, Part A as illustrated in Fig. 4, obtains a good approximation for the initial heat transfer coefficients on each wall surface and the second, Part B in Fig. 4, is the main loop of the iteration and employs the full 3-D heat conduction in the wall. Two approaches have been used to obtain initial values for the heat transfer coefficients. One, as shown in Part A, is based on the previous 1-D wall model and is described as follows. (The second, discussed in Section 4.1, is based on an arbitrary choice of an initial wall temperature, for example the mean of the temperature of the coolant and of the hot gas.)

The primary flow, cooled by the coolant jets, is first solved assuming an adiabatic wall. The computed adiabatic wall temperature is then imposed as a temperature boundary condition for the backside coolant flow. Once the backside flow (including flow through the hole) reaches a steady state, the heat flux through the backside wall surface and through the hole inner surface can be calculated and from this the backside heat transfer coefficient h_2 and internal heat transfer coefficient h_3. At this point, h_2 is used to solve the primary flow with the thermal boundary condition given by Eq. (4), as proposed in the 1-D wall model of Zhong and Brown. Using Eq. (4) in this way and the temperature and velocity profiles at the exit of the hole obtained by solving the backside flow, a new temperature T_{w1}, heat flux q_{w1} and h_1 on the upper wall surface can be calculated. These calculated distributions of h_1, h_2 and h_3 are then used as the initial values in the boundary conditions, which are used to solve the heat conduction equation as in Part B of Fig. 4.

Solving the heat conduction equation with the mixed boundary conditions, Eqs. (5)–(7), provides the distribution of temperature and heat flux inside the wall. With

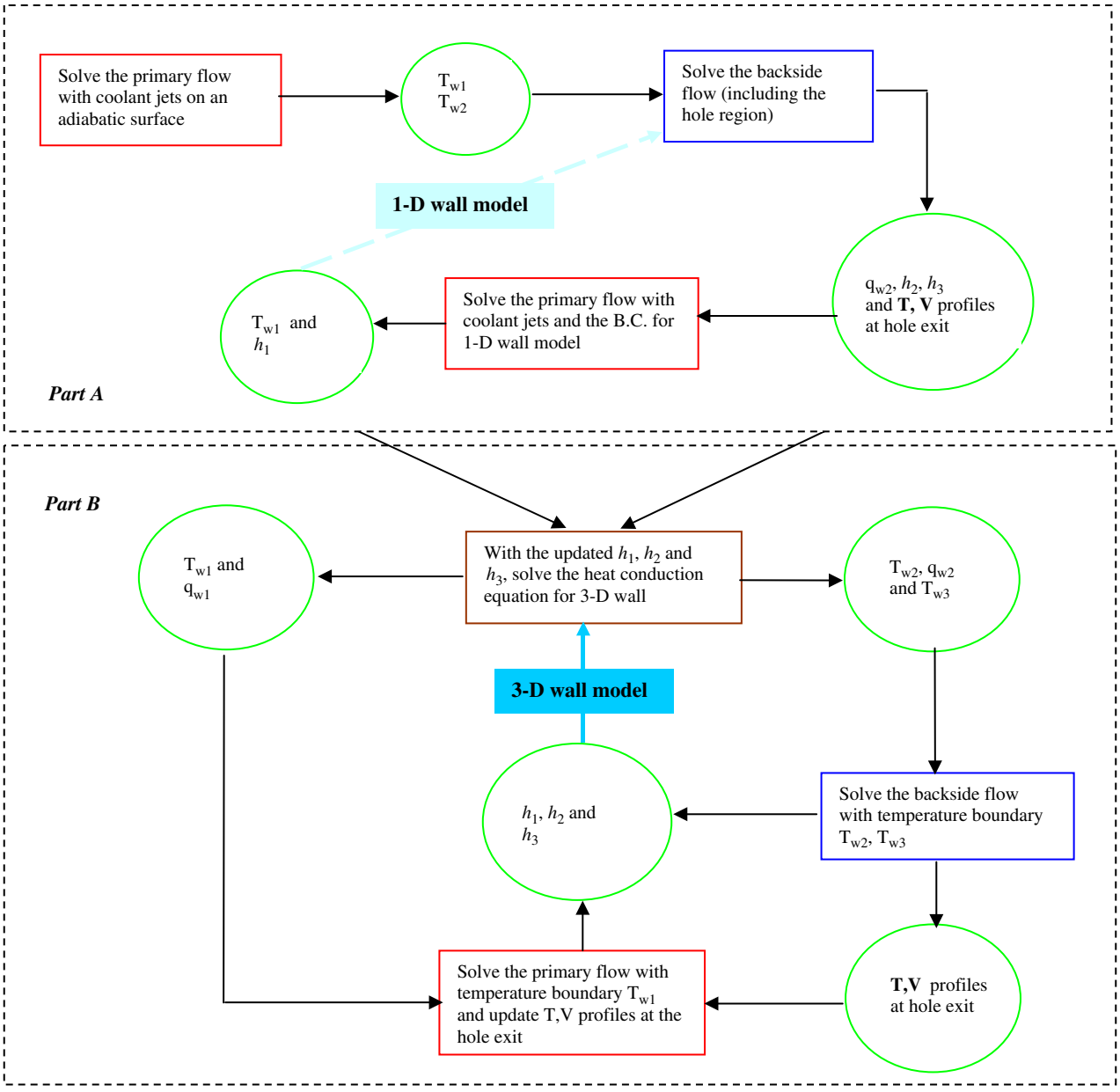

Fig. 4. Flow chart of the iterative process (variables in bold represents the data for fluid/solid communication).

the new wall temperatures: T_{w1}, T_{w2}, T_{w3}, obtained from the 3-D heat conduction equation, which are now used as the temperature boundary conditions for the flow regions, new calculations of the primary flow and of the backside flow give new heat fluxes and new estimates for h_1, h_2, h_3 on the cooling surface, the backside surface and the hole inner surface. The updated h_1, h_2, h_3 are then used to solve the 3-D heat equation again. The iterative steps are repeated until both the wall temperature and the surface heat flux have converged within an acceptable error. Fig. 4 is a flow chart representing the whole process. The mixed boundary condition, small changes with each iteration in the heat transfer coefficients and the uniqueness of the solution to the 3-D heat conduction equation ensure rapid convergence.

3. Numerical methods

The numerical schemes are based on the finite difference method and the DNS calculations used a code developed by Martin et al. [6,7], as discussed in Zhong and Brown [5]. The bandwidth optimized 5th-order scheme with slight upwind characteristics, proposed by Jiang and Shu [8] for the development of a low dissipation "essential non-oscillation (ENO)" scheme, is applied for the approximation of the convective terms in the Navier–Stokes equations. The standard 4th-order central scheme is applied for the viscous terms and the third-order Runge–Kutta method for the time terms. The solution is regarded as having reached a steady state when no significant change in the surface temperature or heat flux is observed after taking an average

over a length of time that is long compared with the characteristic time of the velocity fluctuations. The second-order derivative terms in the heat conduction equation are approximated by a standard second-order central scheme and the interpolation of the data at the fluid–solid interface is implemented via weighting functions evaluated by the distance between fluid and solid grid points; the overall accuracy is second-order. While not as highly resolved as it could be, for the present purpose we have used a mesh resolution for the near wall turbulent flow of $\Delta x^+ = 11.5$, $\Delta z^+ = 9.8$ in the streamwise and spanwise directions respectively, and in the normal direction, the first grid point away from the wall is at $\Delta y^+ = 0.2$ and there are 19 grid points located below $y^+ = 10$. The computational domain is $10.5\delta_{0.99}$ ($\delta_{0.99}$ is the inlet boundary layer thickness) in the x direction, $2.4\delta_{0.99}$ in the z direction and $4.4\delta_{0.99}$ in the y direction. The corresponding length and width of each hole are shown in Table 2, for which the non-dimensional length and width are 43 and 29, in wall units ($\frac{\nu}{u_\tau}$) respectively. We impose zero normal gradients at the upper surface of the computational domain boundary and no-slip conditions for the velocity boundary condition at the wall. The velocity and temperature profiles calculated by solving the backside cavity flow are imposed at the hole in the plane of the upper wall surface for the flow above this surface. At the downstream boundary, a convective boundary condition of the form $\frac{\partial u_i}{\partial t} + \overline{U}\frac{\partial u_i}{\partial x} = 0$ is applied, where, $\overline{U}$ is the local bulk velocity.

4. Tests of the model

4.1. A test case with a laminar primary flow and a single hole

As a first test of the method, a laminar boundary layer flow over a flat plate with a single row of coolant jets was calculated. The rectangular injection hole in this case is normal to the surface and the coolant flows perpendicularly towards the backside wall surface. Fig. 5(a) gives a schematic diagram of the cooling system and Fig. 5(b) gives a side view and the dimensions. Table 1 gives the parameters for this case. The thermal conductivity, specific heat and density are the values for the ceramic matrix composite specimen used in the later experiments. No experiment was performed with a laminar flow and a single row of holes. The dimensions of the hole are approximately those of the ceramic matrix specimen and the holes are approximately

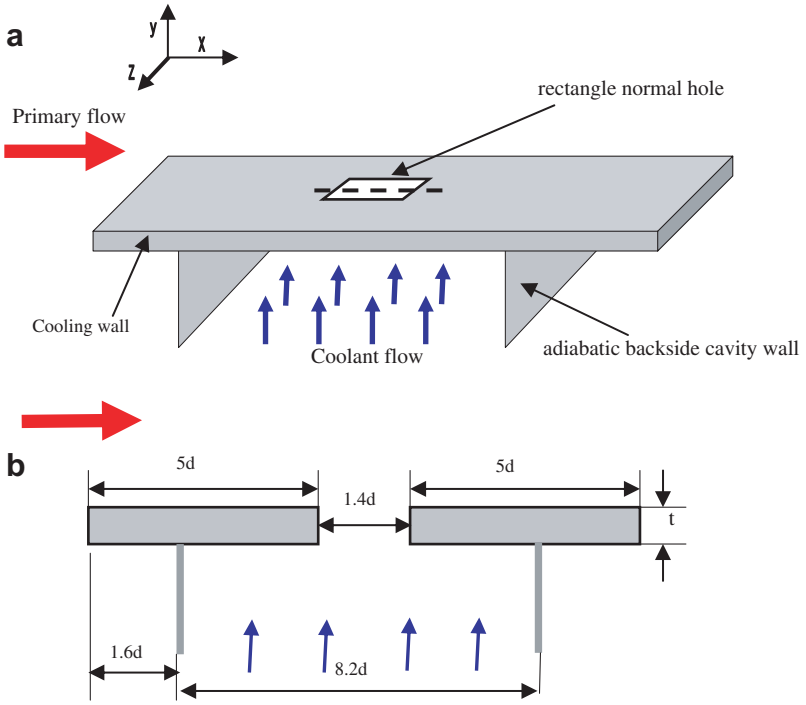

Fig. 5. Schematic view of the multi-hole cooling configuration.

Table 1
Flow and wall properties for the laminar cooling cases

Flow condition	*Re* at domain inlet	2.5E04	Free stream temperature (K)	360	Free stream velocity (m/s)	20
	Coolant temperature (K)	300	*M* (blowing ratio)	0.15	$\delta_{0.99}$ (mm)	0.91
Wall material	Thermal conductivity (W/m K)	4.5	Density (kg/m^3)	4000	Specific heat (J/kg K)	700
Wall geometry	Injection hole	Rectangle	Hole size (mm) (length × width)	1.3 × 0.72	*t* (mm)	1.5
	P (mm)	1.8	Injection angle	90	*d* (mm)	0.93

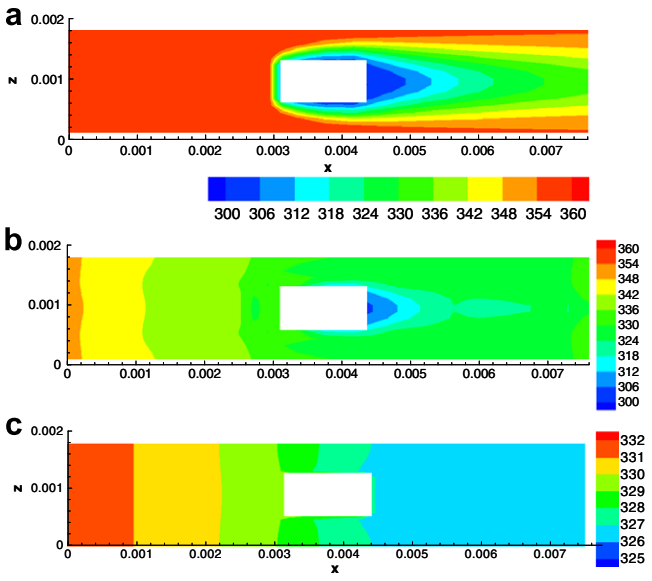

Fig. 6. Surface temperature contours (a) adiabatic model; (b) 1-D coupled model [5]; (c) 3-D coupled model (blank regions denote the injection hole, (c) have a different temperature scale from figure (a) and (b)).

rectangular as a result of the woven material and the process used to generate the holes.

Fig. 6[2] is the cooling surface temperature calculated with three different wall models: (a) an adiabatic wall, (b) a 1-D conducting wall and (c) the 3-D conducting wall. Compared to the adiabatic wall model, the other two models give significantly lower surface temperatures; the comparison demonstrates the additional cooling effect due to backside and internal cooling. The most important difference between the 1-D and the 3-D wall model is the much smaller temperature variation on the cooling surface obtained with the 3-D wall model. This shows, in this case, that there is a significant horizontal heat flux, which acts to smooth out the surface temperature. Fig. 7(a) and (b) shows the heat flux vectors on the cooling surface and on an x–y plane along the hole centerline (obtained from the 3-D solution) with the temperature contours as a background. Not unexpectedly the horizontal heat flux component becomes a larger fraction of the heat flux around the injection hole, and clearly here the 1-D heat flux assumption is inaccurate.

The convergence to the solution is evident in Fig. 8 where the spanwise-averaged surface temperatures (excluding the hole) have been plotted after each iteration step. For this cooling case, only three steps (one in Part A, two in Part B) are necessary to reach a converged solution. Fig. 9(a) and (b) shows the spanwise-averaged heat transfer coefficients h_1 and h_2 calculated in each fluid region at each step. The convergence of the solution is again confirmed and h_2 may be seen to converge faster than h_1 (as might be expected because of the small region where h_1 is either

[2] *Note*: Figures with the x-coordinate starting from zero define the origin at the upstream boundary of the backside cavity as shown in Fig. 5.

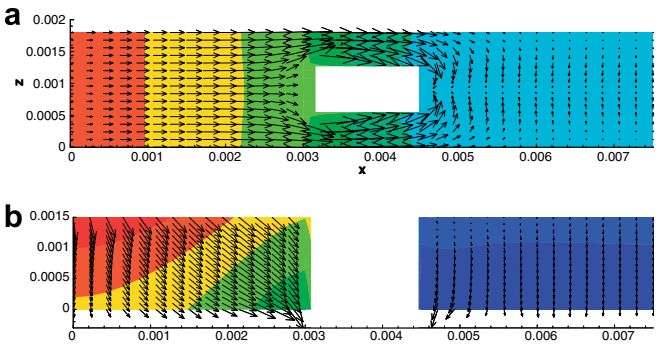

Fig. 7. Heat flux vector (a) on the cooling surface; (b) on the x–y plane through the centerline.

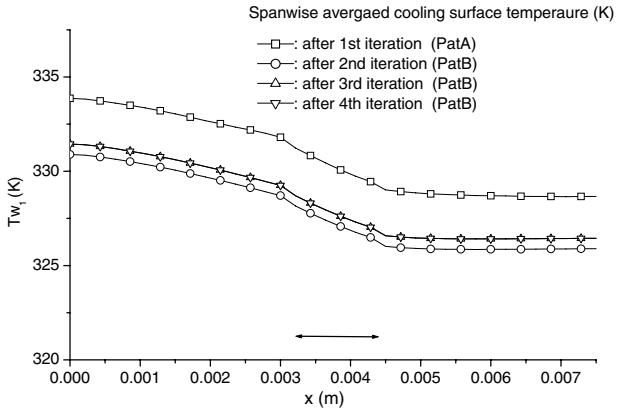

Fig. 8. Spanwise-averaged cooling surface temperature (the bar denotes the hole location).

negative or it has a relatively small positive value, see Section 2.2).

We note that, instead of using the 1-D model to obtain initial estimates for h_1, h_2, h_3, we can begin by imposing an arbitrary constant temperature boundary condition, for instance, $T_{w1} = T_{w2} = \frac{1}{2}(T_\infty + T_c)$. The flow in the two regions can then be computed to find h_1, h_2, h_3 which may then be used as initial estimates with the 3-D heat conduction equation to find new distributions for the wall temperature and the iteration (Part B in Fig. 4) can again proceed. When tested with this laminar case again only three iteration steps were necessary to reach a converged solution.

4.2. A test case with a turbulent primary flow and three rows of downstream holes

The 3-D model was also tested with a turbulent boundary layer as the primary flow and in this case with three downstream rows of injection holes. The Reynolds number based on the upstream boundary layer momentum thickness, Re_θ, was chosen to be 620. The corresponding Re_x (or Re) assuming a flat plate is approximately 200,000. For this computational case, the free stream turbulence level is essentially zero. The DNS calculation of the turbu-

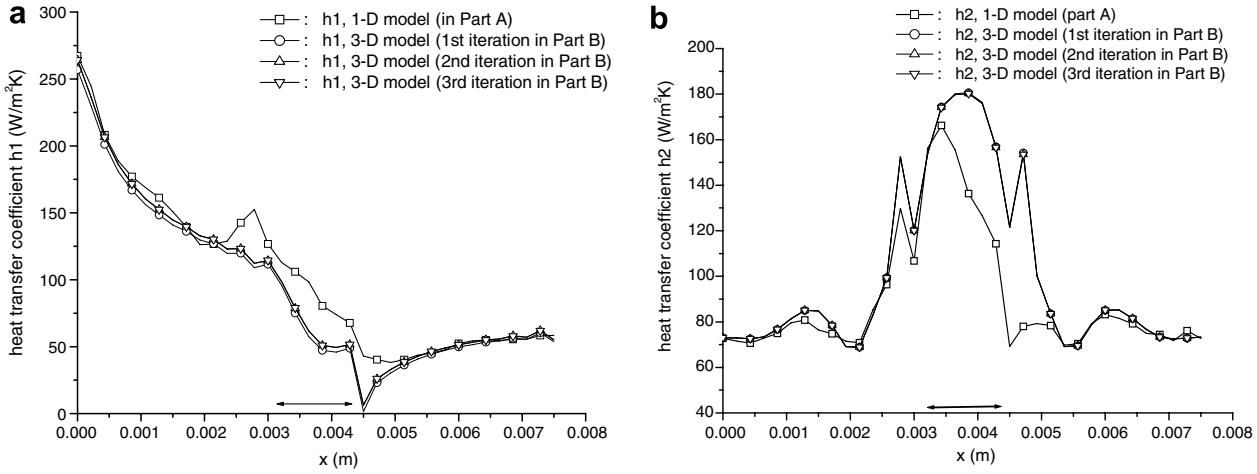

Fig. 9. Spanwise averaged heat transfer coefficients at each iteration step (a) h_1 and (b) h_2.

lent boundary layer flow was generated by imposing, at an upstream flow boundary, a mean turbulent velocity profile (obtained by a RANS calculation with a Baldwin–Lomax turbulence model at the same Re_θ) plus steady, three-dimensional, velocity perturbations comparable in magnitude with the classical, experimentally measured, rms values at this Re_θ. Such a steady velocity distribution in the boundary layer will be unstable and the computed boundary layer will rapidly become turbulent. Ideally, in the calculation, the turbulent boundary layer would be allowed to develop over a large length. For the purpose of this test the development length was only $8\delta_{0.99}$, but even at this location the Reynolds stress and rms turbulent velocity fluctuations were relatively close (Fig. 10) to those

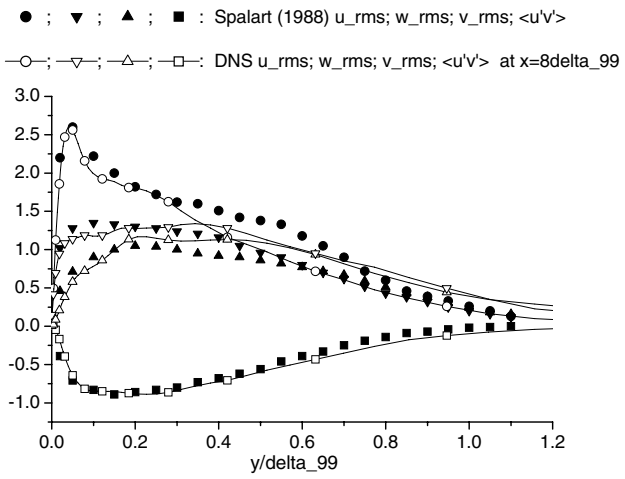

Fig. 10. Fluctuations compared with results from [9].

of more extensive DNS calculations at a comparable Re_θ [9]; the cooling holes were then located downstream of this development length with three holes located in the streamwise direction and six holes in the spanwise direction. The ratio of the boundary layer thickness to the holes size (d) was approximately 8.

Table 2 gives the flow conditions, the wall geometry and locations of the holes etc. The properties of the wall material are the same as those in the laminar case. The shape, size and spacing of the holes used in the DNS calculation are chosen to be close to those of the CMC panel used in the experiments in the wind tunnel. In the calculation, the wall temperature and heat flux used to calculate the heat transfer coefficient were time-averaged (obtained by averaging the calculated local values over a period of 2–5 $\frac{\delta_{0.99}}{U_\infty}$). It is important to appreciate that the coupling between the two flow regions and the wall is through mean values and any additional heat transfer, for example, resulting from static pressure fluctuations and unsteady flow in the cooling holes, is not being captured. (For a mean pressure drop along the streamlines through the cavity, which is large compared with the level of the rms static pressure fluctuations, we expect the approximation of coupling with mean values to be relatively good, but this aspect has not yet been studied in detail.) Two injection cases were considered, one with a low blowing ratio $M = 0.25$ and the second with a moderate blowing ratio $M = 0.43$.

For this turbulent case, the adiabatic boundary condition at the upstream boundary of the wall is replaced by a boundary condition that more closely represents the experimental condition. Fig. 11 shows the experimental configuration. A ceramic holder with a length of 10 mm

Table 2
Flow and wall properties for the turbulent cooling cases

Flow condition	*Re* at domain inlet	2E05	Free stream temperature (K)	300	Free stream velocity (m/s)	10
	Coolant temperature (K)	250	*M* (blowing ratio)	0.25, 0.43		
Wall geometry	Injection hole size (mm)	1.35, 0.92	Injection angle	90	*t* (mm)	1.5
	P (mm)	2.8	*S* (mm)	6.6	*d* (mm)	1.06

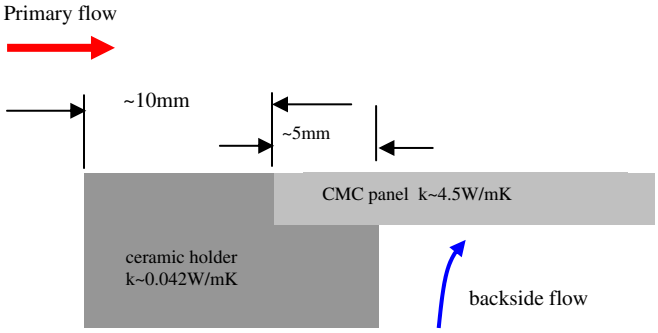

Fig. 11. The improved upstream boundary condition.

is used to locate the multi-hole panel and to insulate it from the metal tunnel walls. The thermal conductivity of the ceramic holder is approximately 0.042 W/m K, which is much lower than that of the cooling panel. An isothermal boundary condition with $T = T_\infty$ is then applied at the upstream edge of the ceramic holder. The ceramic holder and the part of the wall panel attached to it where there is no-backside-flow are all included in the 3-D, heat conduction solver.

Fig. 12 shows results for the $M = 0.25$ case. In particular, it shows the converged cooling surface temperature (spanwise-averaged, excluding the hole) calculated with

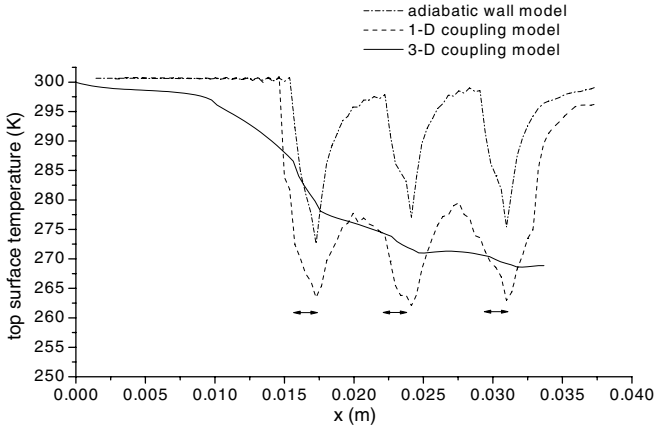

Fig. 12. Spanwise-averaged cooling surface temperature (bar denotes the hole location) for the turbulent cooling case $Re \sim 200{,}000$.

an adiabatic, a 1-D and the full 3-D, wall model. Compared with the adiabatic wall model, the lower surface temperatures obtained with the 1-D and 3-D models confirm the considerable contribution to the overall effectiveness of backside and internal cooling for this cooling system. The surface temperature obtained with the 3-D model is much smoother than obtained with the 1-D model which confirms the significant role played by in-plane conduction in the wall. The result of the 3-D model also indicates the effectiveness of the ceramic holder as an insulator for the cooling panel since there is only a small temperature drop along the holder upstream of the panel. The surface temperature curves show the approach towards a periodic temperature distribution with respect to each row of holes. Fig. 13(a) gives the cooling surface temperature contours at $M = 0.25$. The temperature is relatively uniform due to the strong in-plane heat conduction and the relatively large open area for this specific cooling panel at this Reynolds number. Fig. 15(a) shows the heat flux vector in the wall on an x–y plane through the centerline of the holes and the corresponding temperature contours obtained from the 3-D solution. The horizontal heat flux is significant, especially in the vicinity of each hole. For this turbulent test case, the solution with the 3-D model converges quickly and only three iteration steps (in Part B of Fig. 4) were required.

It is possible to extend, approximately, the application of the current DNS calculation to a cooling system at higher Reynolds number if we assume that the local Stanton numbers (St) of both the primary and the backside flows are weakly dependent on the Reynolds number. If we keep the same mass flow rate ratio and the same cooling configuration then, as a first approximation, we assume Stanton number does not change with Reynolds number. Thus the local heat transfer coefficient will be proportional to the local mass flow rate: ρu. In particular, the h_1, h_2 and h_3 obtained at low Reynolds number from the current DNS calculation would be modified, as in (8), and then used in the 3-D wall solver for a higher Reynolds number case

$$h_{1,2,3}^{\text{higher } Re} = h_{1,2,3}^{\text{current}} \frac{(\rho u)_{1,2,3}^{\text{higher } Re}}{(\rho u)_{1,2,3}^{\text{current } Re}} = h_{1,2,3}^{\text{current}} \frac{Re^{\text{higher}}}{Re^{\text{current}}} \tag{8}$$

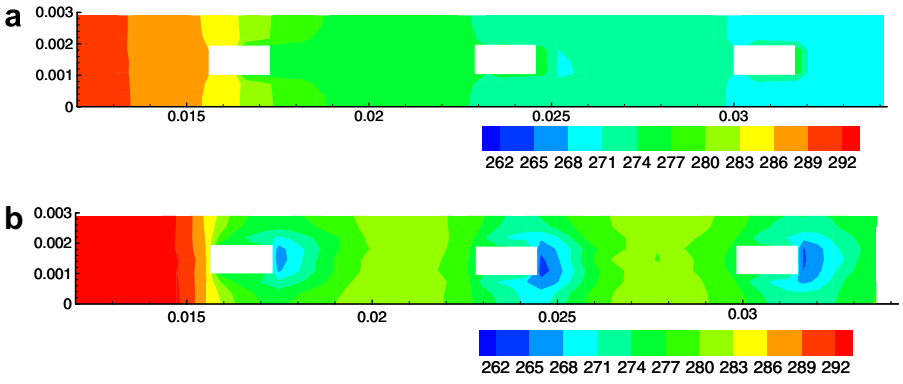

Fig. 13. Cooling surface temperature contours (a) $Re \sim 200{,}000$ and (b) $Re \sim 4{,}000{,}000$.

(For a laminar backside cooling flow, a better approximation for heat transfer coefficient at higher Reynolds number would be $h_2^{\text{higher } Re} = h_2^{\text{current}} \sqrt{\frac{(\rho u)_2^{\text{higher } Re}}{(\rho u)_2^{\text{current } Re}}}$).

Based on the assumption of (8), (that the Stanton number is independent of Reynolds number), Fig. 14 gives the spanwise-averaged cooling effectiveness θ at a blowing ratio of $M = 0.25$ for a range of Reynolds numbers. Fig. 13(b) is the calculated surface temperature at a higher Reynolds number ($Re \sim 4{,}000{,}000$) using the above assumption. It is interesting that there is an increase in the variation of the local cooling effectiveness (i.e. the surface temperature) as Reynolds number increases. This indicates that the 3-D wall model becomes increasingly like the 1-D wall model at higher Reynolds number. To verify that that is the case, the heat flux vector and the isotherms in the wall on the x–y plane through the centerline of the holes are shown in Fig. 15(a) and (b) for $Re \sim 200{,}000$ and $Re \sim 4{,}000{,}000$. Except in the vicinity of the hole, the heat flux vector points mostly downwards for the high Reynolds number case; the heat flux for the low Reynolds number case, however, has a much larger horizontal component.

The approach towards the 1-D model of the 3-D model as Reynolds number increases can be readily explained. When the Reynolds number is increased, the convection of heat from the surface to the fluid is enhanced and thus the relative effect of in-plane heat conduction in the wall is diminished. A non-dimensional parameter, which will represent the relative importance of wall, in-plane, heat conduction, is $\lambda = \frac{ht}{k_w}$ (a Biot number). For the two Reynolds number cases given in Fig. 13 we obtained

$$\lambda_{Re\sim 200{,}000} \sim 0.025, \quad \lambda_{Re\sim 4{,}000{,}000} \sim 0.5$$

where, the value used for h was the mean value over the upper surface of the wall.

From the DNS solution for the primary flow, Fig. 16(a) and (b) shows the ensemble-averaged[3] temperature contours and velocity vectors downstream of the third row of holes on an x–y plane through the hole centerline for a blowing ratio $M = 0.25$. Fig. 17(a) and (b) are for $M = 0.43$. The strong effect of the turbulent mixing, captured by DNS, is very evident in the temperature figures. A comparison between Fig. 16(a) and Fig. 17(a) indicates the effect of the larger blowing ratio, which causes stronger mixing and a greater deficit in the velocity profiles. For both cases, no substantial region of separation of coolant from the wall (in the mean) is calculated. Fig. 18 gives the calculated h_1 at $M = 0.25$. The reduction in h_1 downstream of the holes is evident as also the small region of negative h_1, indicating a negative heat flux to the wall. Fig. 19 is the calculated backside heat transfer coefficient h_2. Note the region of large h_2 in the vicinity of the holes,

[3] "Ensemble average" means the average of each variable at a given time, at the same location with respect to the six hole locations in the spanwise direction.

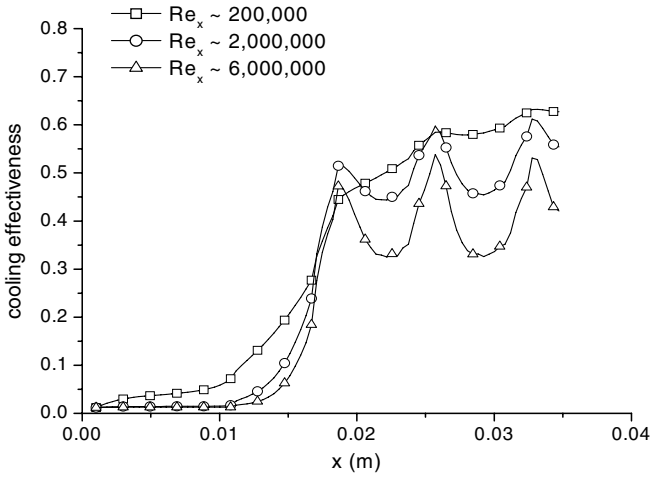

Fig. 14. Cooling effectiveness θ predicted by 3-D model for the cooling system at different Re.

which is a result of the local acceleration of the flow and reduced thermal boundary layer thickness.

As a summary, Table 3 presents the overall cooling performance at the two blowing ratios for the CMC cooling panel that has been studied. All the values in the table have been obtained by taking the average over the whole x–z plane. Two general comments can be made: (1) The front-side heat transfer coefficient h_1 decreases with blowing ratio and the backside heat transfer coefficient h_2 increases. This clearly leads to a lower surface temperature and higher cooling effectiveness with blowing ratio for these two cases. (2) Compared with the overall cooling effectiveness, the adiabatic cooling effect i.e. the effect directly caused by coolant jet/primary flow interaction becomes more important as the blowing ratio increases. The results at higher Reynolds number based on the assumption of constant Stanton number give a corresponding global cooling effectiveness at $Re \sim 4{,}000{,}000$ of 0.35 for $M = 0.25$ and 0.4 for $M = 0.43$ respectively.

4.3. Comparison with experimental results

In parallel with the numerical study, experiments were conducted to investigate the cooling performance for an oxide–oxide CMC cooling panel with multiple rows of normal holes. The specimen is relevant to potential gas turbine applications as discussed by Cox et al. [10]. The special purpose wind tunnel and the experimental arrangement for this study are discussed in detail in Zhong and Brown [5]. In this facility, experiments on a cooling system over a range of Reynolds numbers can be performed simply by keeping the same temperatures and velocities and increasing tunnel pressure from 1 to 20 atmospheres. The whole tunnel has been insulated so that the initial effects of heat loss through the tunnel wall, at low Reynolds number (pressure), have been eliminated to a satisfactory level. Fig. 20 is a photograph of the insulated tunnel and the cooling flow injection system. Fig. 21 is a photograph of

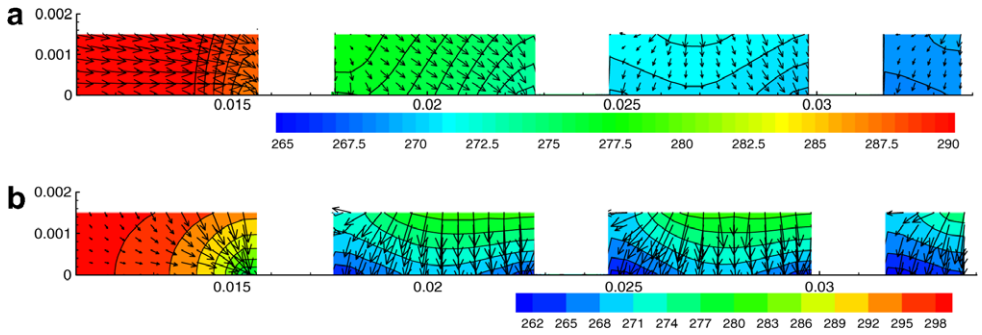

Fig. 15. Heat flux vectors and isotherms on a x–y plane for different Re: (a) $Re \sim 200{,}000$; (b) $Re \sim 4{,}000{,}000$ (vector length in (a) and (b) is not to scale).

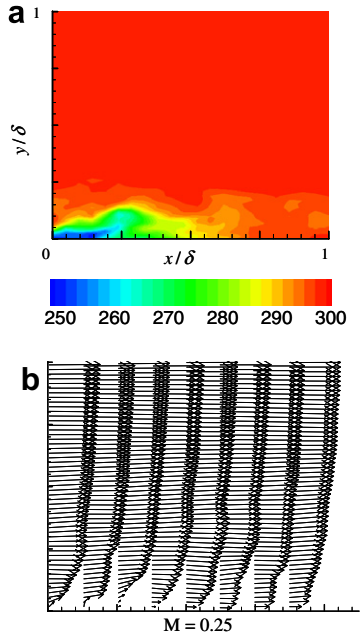

Fig. 16. Temperature contours and velocity vectors downstream of an injection hole on an x–y plane ($M = 0.25$).

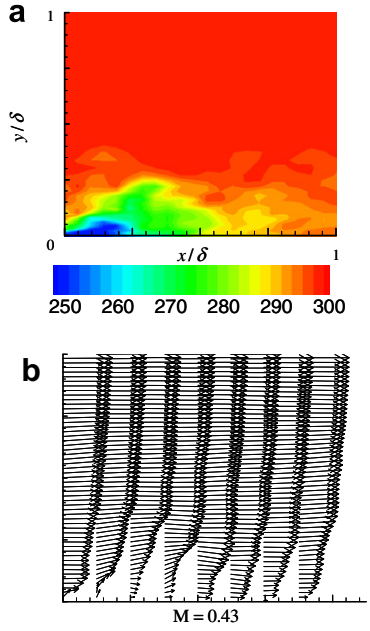

Fig. 17. Temperature contours and velocity vectors downstream of an injection hole on an x–y plane ($M = 0.43$).

the multi-holed ceramic cooling surface. The cooling surface consists of multiple rows of approximately rectangular, normal holes. It is apparent that the holes have a poor uniformity, so an average hole size was chosen for the numerical study. The ceramic panel has a thickness of 1.5 mm and a relatively large percentage open area of 7%. The thermal properties of the material are the same as the values used in the numerical study.

The free stream turbulence level in the tunnel test section was measured and, in the absence of the intended turning vanes, a level of ~2% for $200{,}000 < Re_x < 2{,}000{,}000$ was found. Although free stream turbulence is not considered in the numerical study, the numerical results are compared with the experimental data since at this relatively low free stream turbulence level, the effect on cooling performance is expected to be weak compared with other parameters such as blowing ratio.

Surface temperatures were measured with thermocouples mounted on the cooling surface and velocity and temperature profiles were obtained by traversing a pitot probe and a temperature probe across the boundary layer at the same physical location as in the numerical study (downstream of the third spanwise row). Fig. 22 is a schematic diagram showing the location of the surface temperature measurements and the location for the survey for the velocity and temperature profiles. The backside flow temperature was measured by a thermocouple mounted approximately 6 mm beneath the cooling surface and well outside the backside flow boundary layer. The backside cavity pressure was also measured and used to determine the injection velocity through the hole from the pressure difference between it and static pressure of the primary flow. The uncertainty in the measurement was estimated from measurement resolution and the repeatability of the results and found to be approximately $\leqslant 4\%$ for the cooling effectiveness and $\leqslant 8\%$ for the blowing ratio.

Fig. 23(a)–(d) presents the results for the cooling effectiveness at locations (1)–(4) shown in Fig. 22 at four

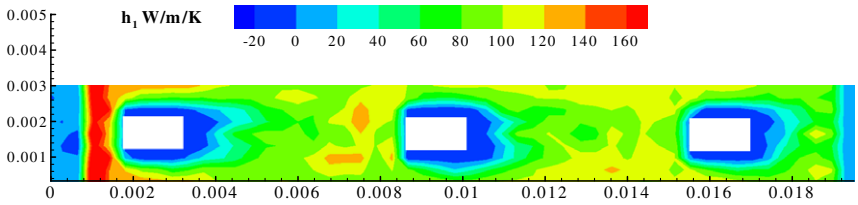

Fig. 18. h_1 on the cooling surface at $M = 0.25$.

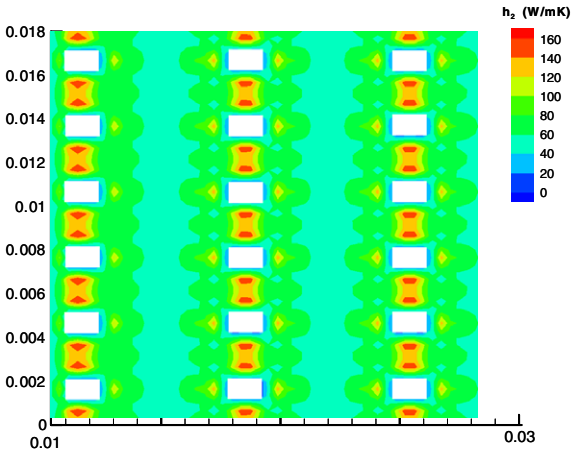

Fig. 19. h_2 on the backside surface.

Fig. 20. Insulated closed-circuit wind tunnel with the secondary flow injection system.

Fig. 21. The multi-holed ceramic surface.

Reynolds numbers. They show the initial increase in the cooling effectiveness with blowing ratio. For $M > 0.7$, however, the cooling effectiveness increases weakly with the blowing ratio. This suggests that a local film of coolant could have been established above the cooling surface at large blowing ratio. A dependence on Reynolds number is observed in the figures (a small reduction in effectiveness with increasing Reynolds number), and the effect is more significant at small blowing ratios and diminishes at large blowing ratios. This can be explained by a combined effect of the backside cooling and heat conduction in the wall. When the backside cooling effect is significant (for small blowing ratio), the increase in the system Reynolds number, i.e. the system pressure and density, increases the transport of heat in the flow regions, which then increases the heat flux through the wall and causes the temperature drop across the wall to become larger and raises the upper surface temperature. The numerical results at two low-to-moderate blowing ratios, discussed in the last section, are consistent with this Reynolds number dependence.

Results of the temperature measurements for two blowing ratios ($M = 0.25$, $M = 0.43$) and a direct comparison between the measured and calculated cooling effectiveness (using the 3-D procedure of this paper) are shown in Fig. 24(a). A comparison between measurements at other Reynolds numbers and predictions based on the constant Stanton number approximation are shown in Fig. 24(b). As shown in these figures, the numerical predictions agree well with the experimental results. (The experimental specimen has a variation in the size of the holes, which has not been modeled, and there are other experimental and numerical factors such as the roughness of the real specimen, which could account for the remaining difference.) In Fig. 24(b), the small under-prediction of the cooling effectiveness

Table 3
Overall cooling performance for the CMC cooling panel

Blowing ratio	Global h_1 (W/m^2 K)	Global h_2 (W/m^2 K)	Global cooling effectiveness	Gobal adiabatic cooling effectiveness
0.25 ($Re \sim 200{,}000$)	71.3	80.5	0.45	0.14
0.43 ($Re \sim 200{,}000$)	55.2	103.2	0.51	0.23

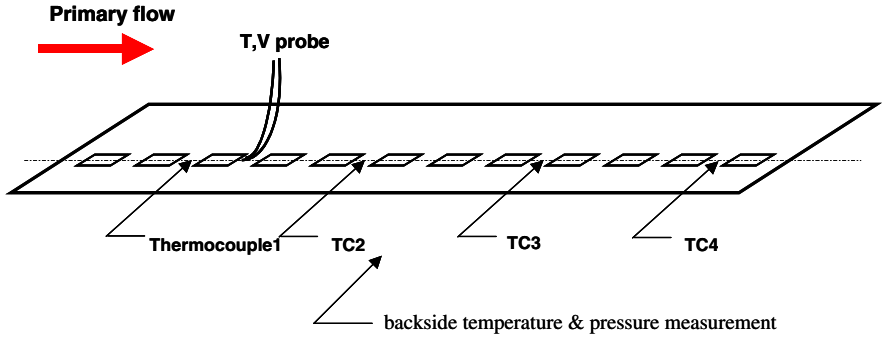

Fig. 22. A schematic diagram showing locations of surface temperature measurements and T, V probes.

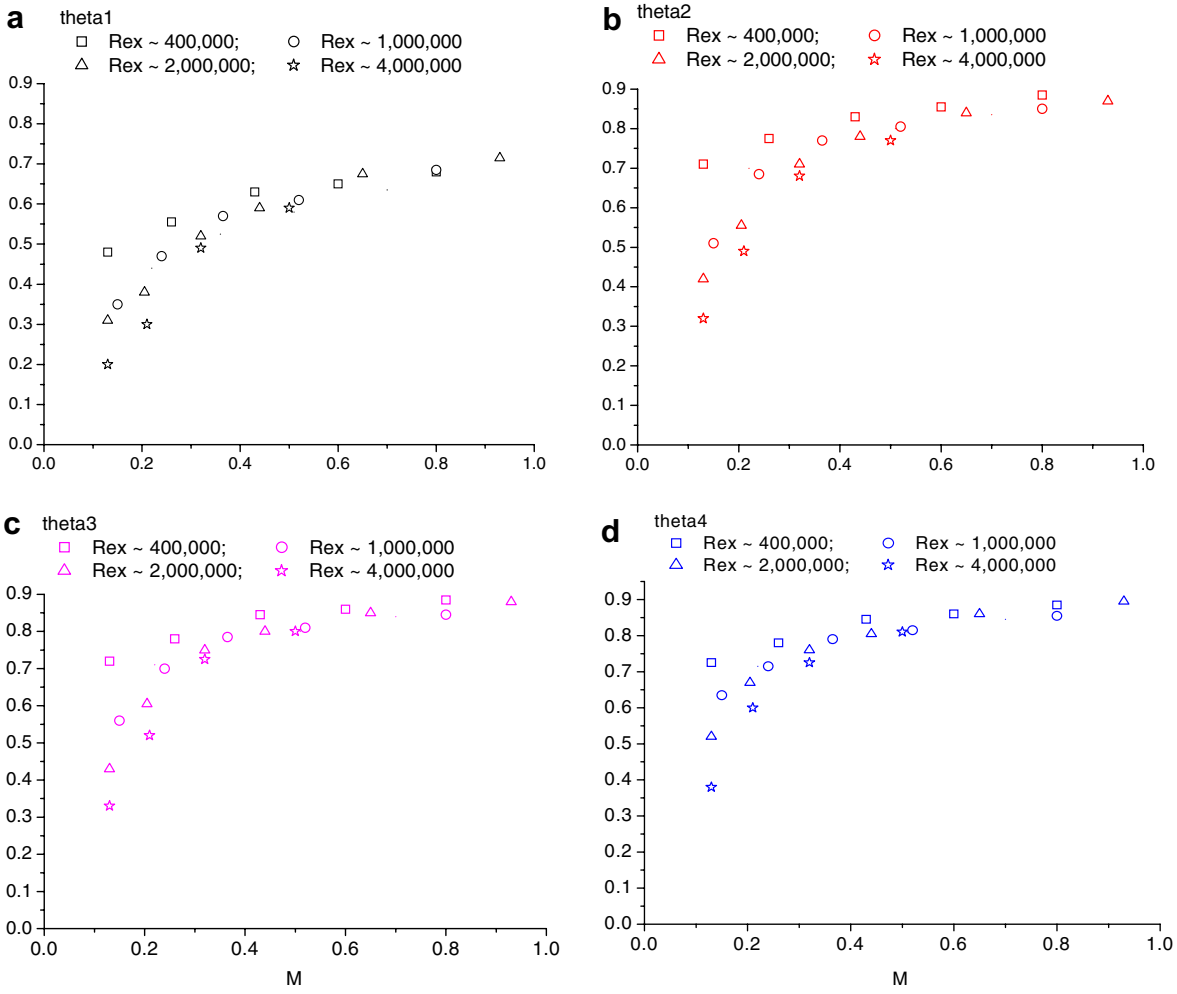

Fig. 23. Cooling effectiveness as a function of blowing ratio at four streamwise locations and at different Reynolds numbers (a) location 1; (b) location 2; (c) location 3; (d) location 4.

observed for the higher blowing ratio case and over-prediction for the lower blowing ratio case could be a result of the approximation of constant Stanton number that is used for the heat transfer coefficients at higher Re, or possibly an effect of the idealized upstream boundary condition used when solving the 3-D heat conduction equation.

In Fig. 25(a) and (b) the measured velocity and temperature profiles are compared with the numerical results at the same physical location. They agree with each other satisfactorily. The agreement between the measured temperature profile and the numerical prediction, using the 3-D heat transfer model rather than 1-D model, is now significantly better than it was previously in Zhong and Brown [5]. Apart from the model improvement, the tunnel has now been well insulated so that the previous initial heat transfer through the tunnel wall has been substantially reduced.

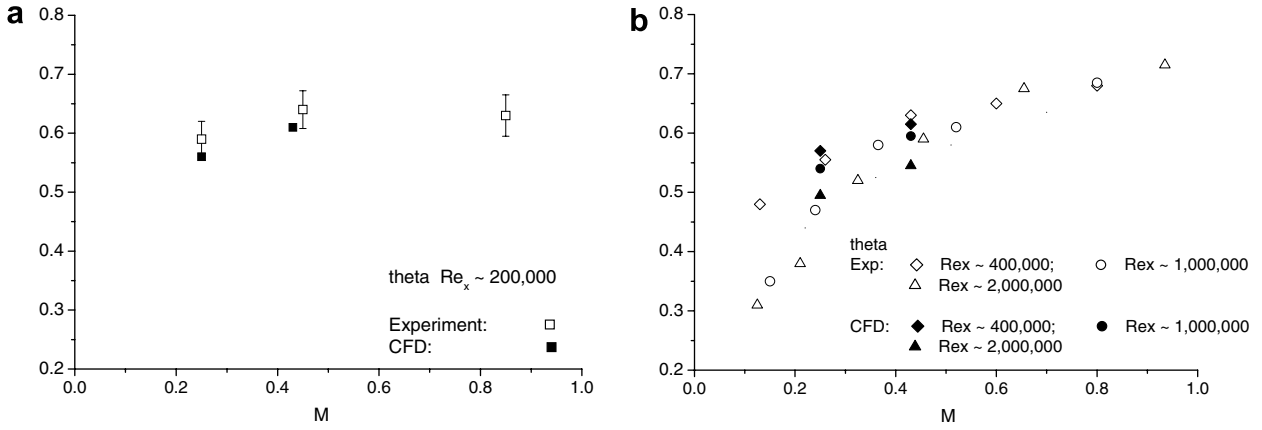

Fig. 24. Comparison of cooling effectiveness θ between experiment and the 3-D model (a) $Re \sim 200{,}000$; (b) higher Reynolds numbers.

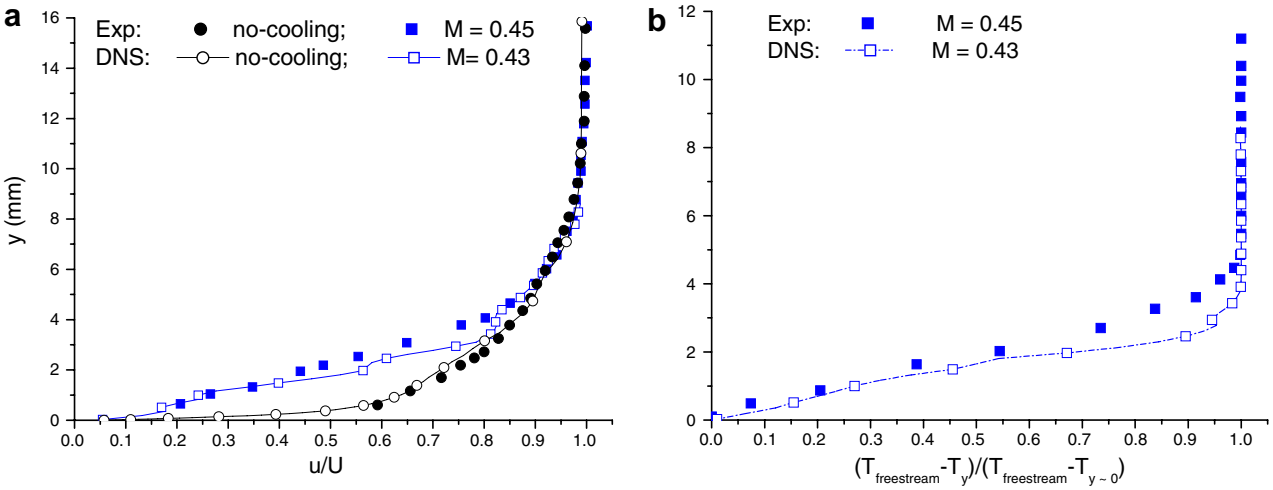

Fig. 25. Comparison of velocity and temperature profiles by experiment and DNS solution (a) velocity, w/wo cooling; (b) temperature.

5. Conclusions

In the present study, a 3-dimensional, coupled, DNS heat transfer model is introduced and applied to investigate a multi-hole, woven CMC cooling surface. Based on the results, the following conclusions can be drawn:

1. The mixed boundary condition governed by a local heat transfer coefficient on all surfaces is proposed for the full 3-D coupling because of the weak dependence of the heat transfer coefficient on the surface temperature. It is proved that uniqueness is guaranteed only if the heat transfer coefficient is positive. In the small region on the surface where it is not positive the local heat flux is used. In this case it is also proved that the boundary conditions guarantee the uniqueness of the solution of the steady heat conduction equation. The methodology, which couples the fluid flow and the conduction in the wall by exploiting this boundary condition can therefore be expected to achieve rapid convergence.
2. The 3-dimensional model with its iteration procedure is found to converge quickly and a converged solution for the temperature field in the wall can be obtained in less than 3–4 iteration steps.
3. The cooling effectiveness obtained with the 3-dimensional model is much higher than that for an adiabatic wall model. This implies that the backside cooling and internal cooling, for the CMC cooling panel at blowing ratios of 0.25 and 0.43, plays a substantial role.
4. The 3-dimensional model reveals significant in-plane heat conduction in the wall and a much smaller variation in surface temperature when compared with the 1-dimensional wall model.
5. The 3-dimensional wall model approaches the 1-dimensional wall model as the Reynolds number is increased and a Biot number is chosen as a parameter that represents the relative importance of the in-plane heat conduction.
6. The cooling effectiveness predictions, found with the DNS flow calculations and the 3-dimensional heat conduction model, agree well with the experimental results and the technique of extending the current low Reynolds number DNS results to higher Reynolds number cases has proven to be a reasonable first approximation.

The three-dimensional, coupled, DNS approach can now be used to answer many questions on the optimal geometry of the cooling holes, on the details of the physical flow field and heat flux in the neighborhood of holes, on comparisons with conventional engineering models and on effects of the temperature ratio etc.

The current model, however, is based on coupling mean variables and it therefore can not follow transient cooling processes. A possible modification of the current model to include transient aspects is to solve the flow field by DNS and the unsteady heat conduction equation in the solid wall and to couple them simultaneously. This, of course would be an expensive computation, but it offers the prospect of providing information from which thermal strains, caused by temperature and heat flux fluctuations, could be calculated. It is a principal objective for future work.

Acknowledgements

The authors would like to thank the Air Force Research Laboratory, Rockwell Science Center and TK Engineering for their support and interest in this work. The authors would also like to thank particularly Professor M.P. Martin for her generosity in allowing us the use of her CFD code and Professor L. Martinelli for his help and support in providing computing time on his parallel computation facility.

Appendix A

Consider the Laplace equation, $\nabla^2\varphi = 0$, with a mixed boundary condition of the general form

$$a\varphi + b\frac{\partial\varphi}{\partial n} = c \tag{A-1}$$

where, a, b, c are coefficients which can be functions of space on the boundary.

If we define $\vec{v} = \nabla\varphi$ and since $\nabla\cdot\vec{v} = 0$

$$\int \nabla\cdot(\varphi\vec{v})\,\mathrm{d}V = \int |\vec{v}|^2\,\mathrm{d}V \tag{A-2}$$

Then using Gauss' Theorem, we have

$$\int |\vec{v}|^2\,\mathrm{d}V = \int \varphi\vec{v}\cdot\vec{n}\,\mathrm{d}S \tag{A-3}$$

If we assume φ and φ' are two distinct solutions which satisfy the same boundary condition, then the linearity of the Laplace equation requires that $\varphi - \varphi'$ is also a solution. Thus as in (A-3)

$$\int |\vec{v}-\vec{v}'|^2\,\mathrm{d}V = \int (\varphi-\varphi')(\vec{v}-\vec{v}')\cdot\vec{n}\,\mathrm{d}S = \int (\varphi-\varphi')(\nabla\varphi-\nabla\varphi')\cdot\vec{n}\,\mathrm{d}S \tag{A-4}$$

Then Eq. (A-4) can be rewritten as

$$\int |\vec{v}-\vec{v}'|^2\,\mathrm{d}V = \int (\varphi-\varphi')\left(\frac{\partial\varphi}{\partial n}-\frac{\partial\varphi'}{\partial n}\right)\mathrm{d}S \tag{A-5}$$

With the mixed boundary condition (A-1) substituted into Eq. (A-5), we have

$$\int |\vec{v}-\vec{v}'|^2\,\mathrm{d}V = \int -\frac{a}{b}(\varphi-\varphi')^2\,\mathrm{d}S \tag{A-6}$$

Thus, when $\frac{a}{b} \geqslant 0$, the equality of the left and right-hand sides of Eq. (A-6) is only possible if both sides are equal to zero, which ensures that $\nabla\varphi = \nabla\varphi'$ everywhere within the volume and $\varphi = \varphi'$ on the boundary, so that, upon integration, $\varphi = \varphi'$ everywhere within the volume and on the boundary, i.e. the boundary condition with $\frac{a}{b} \geqslant 0$ ensures a unique solution.

Now, rewriting the mixed BC (1) of Eq. (5), $-\frac{\partial T}{\partial n}\big|_{\mathrm{w1}} = \frac{h_1}{k_\mathrm{w}}(T_{\mathrm{w1}} - T_\infty)$, for example, in the form of Eq. (A-1), then the ratio $\frac{a}{b}$ is $\frac{h_1}{k_\mathrm{w}}$, and hence $h_1 \geqslant 0$ is required for the uniqueness of the solution for the temperature field T. Similarly, we find that h_2 and h_3 are required to be non-negative.

In fact, we find small regions where $h_1 < 0$ and then we replace the mixed BC with the actual heat flux q^f_{w1} in this region. This, too, guarantees a unique solution since if the area over which $h_1 < 0$ is S_1 then Eq. (A-4) can be rewritten as

$$\int |\vec{v}-\vec{v}'|^2\,\mathrm{d}V = \int_{S-S_1} (\varphi-\varphi')(\nabla\varphi-\nabla\varphi')\cdot\vec{n}\,\mathrm{d}S + \int_{S_1} (\varphi-\varphi')[(\nabla\varphi-\nabla\varphi')\cdot\vec{n}]\,\mathrm{d}S \tag{A-7}$$

If $\nabla\varphi = \nabla\varphi'$ on the boundary of S_1 (as imposed by the heat flux q^f_{w1} on the boundary), the second term on the right-hand side of Eq. (A-7) is zero, so that again, we have

$$\int |\vec{v}-\vec{v}'|^2\,\mathrm{d}V = \int_{S-S_1} -\frac{a}{b}(\varphi-\varphi')^2\,\mathrm{d}S \tag{A-8}$$

and since $\frac{a}{b} \geqslant 0$ on the surface $S - S_1$, then as above, the equality of the left and right-hand sides of Eq. (A-8) is only possible if both sides are zero. Thus, we have $\nabla\varphi = \nabla\varphi'$ everywhere within the volume and $\varphi = \varphi'$ on the boundary of $S - S_1$ and also $\nabla\varphi = \nabla\varphi'$ on S_1. Thus, upon integration, $\varphi = \varphi'$ everywhere within and on the boundary (assuming continuity of φ) and the solution is therefore unique.

References

[1] Y. Lin, B. Song, B. Li, G. Liu, Z. Wu, Investigation of film cooling effectiveness of full-coverage inclined multi-hole walls with different hole arrangements, GT2003-38881, in: Proceeding of ASME Turbo Expo 2003 Atlanta, GA.

[2] T.F. Fric, R.P. Campbell, M.G. Rettig, Quantitative visualization of full-coverage discrete-hole film cooling, ASME Paper 97-GT-328, 1997.

[3] B. Leger, P. Miron, J.M. Emidio, Geometric and aero-thermal influences on multi-holed plate temperature: application on combustor wall, Int. J. Heat Mass Transfer 46 (2003) 1215–1222.
[4] M. Martiny, A. Schulz, S. Wittig, Mathematical model describing the coupled heat transfer in effusion cooled combustor walls, ASME Paper 97-GT-329.
[5] F. Zhong, G.L. Brown, Experimental and numerical studies of multihole cooled ceramic matrix composite liners, AIAA-2005-0184.
[6] M.P. Martin, V.G. Weirs, D. Olejniczak, G.V. Candler, DNS of reacting hypersonic turbulent boundary layers, AIAA-1998-2817.
[7] M.P. Martin, G.V. Candler, Effect of chemical reactions on decaying isotropic turbulence, Phys. Fluids 10 (July) (1998) 1715–1724.
[8] G. Jiang, C. Shu, Efficient implementation of weighted ENO schemes, J. Comput. Phys. 126 (1996) 202–228.
[9] P.R. Spalart, Direct simulation of a turbulent boundary layer up to $R_\theta = 1410$, J. Fluid Mech. 187 (1988) 61–98.
[10] B.N. Cox, J.B. Davis, D.B. Marshall, Q.D. Yang, Integral textile ceramic composites for turbine engine combustors, GT-2002-30056, ASME Turbo Expo 2002, Amsterdam, The Netherlands.